Journal of the European Ceramic Society 40 (2020) 5466–5474

Contents lists available at ScienceDirect

Journal of the European Ceramic Society

journal homepage: www.elsevier.com/locate/jeurceramsoc

Original Article

Excellent energy-storage performances in La_2O_3 doped (Na,K)NbO_3-based lead-free relaxor ferroelectrics

Yanpu Zhang, Ruzhong Zuo*

Institute of Electro Ceramics & Devices, School of Materials Science and Engineering, Hefei University of Technology, Hefei, 230009, PR China

ARTICLE INFO

Keywords:
Energy storage
Lead-free ceramics
Relaxor ferroelectrics
Temperature stability

ABSTRACT

Relaxor ferroelectric (FE) materials have received increasing attention owing to their great potentials for energy-storage applications, especially for the ones with high energy-storage density, efficiency and thermal stability simultaneously. A novel lead-free $[(Na_{0.5}K_{0.5})_{0.97-x}Li_{0.03}](Nb_{0.94-x}Sb_{0.06})O_3$-$xBi(Zn_{1/2}Zr_{1/2})O_3$ (NKLNS-xBZZ) ceramics was developed by a solid-state reaction method. The addition of BZZ has induced obvious dielectric relaxation behavior, as well as improved thermal stability of dielectric response. Furthermore, 0.4 wt.% La_2O_3 was added into the NKLNS-0.06BZZ ceramic, leading to an increased breakdown strength as a result of the reduction of grain size, improvement of bulk resistivity and decrease of dielectric loss. A large recoverable energy-storage density (~4.85 J/cm^3) and a high efficiency (~88.2 %) as well as an excellent thermal stability (± 12 %, 25–140 °C) were simultaneously obtained, together with a fast discharge rate ($t_{0.9}$~112 ns). These results suggest that La_2O_3 doped NKLNS-0.06BZZ ceramic could become an attractive dielectric material for temperature-stable energy-storage capacitors.

1. Introduction

Increasing attention has been recently concentrated on exploiting high-performance dielectric capacitors for energy-storage application owing to the fast development of energy electronics and pulsed power technology [1–3]. Commonly, the energy-storage performances of dielectrics such as recoverable energy-storage density W_{rec} and efficiency (η) can be calculated by the electric field-induced polarization (P-E) hysteresis loops using following equations:

$$W_{rec} = \int_{P_r}^{P_{max}} EdP \quad (1)$$

$$\eta = \frac{W_{rec}}{W} \quad (2)$$

where E is the measured electric field, P_{max} is the maximum polarization and P_r is the remanent polarization [4,5]. A lot of work has been done on improving W_{rec} of various dielectrics including anti-ferroelectrics (AFEs), relaxor ferroelectrics (FEs) and linear dielectrics [6–9]. AFE materials have received wide attention due to their high W_{rec} accompanied by electric field driven AFE-FE phase transition. However, the large hysteresis of AFE-FE and FE-AFE phase transitions also leads to a limited η value [10]. For linear dielectrics, relatively low P_{max} is inherently responsible for the low W_{rec}. Thus, relaxor FE materials with nanodomains have recently received a lot of interests owing to both high W_{rec} and η [11–13].

In the past decades, (Na,K)NbO_3 (NKN)-based perovskites have become one of the most extensively investigated piezoelectric ceramics due to their excellent piezoelectric and ferroelectric properties [14,15]. Moreover, owing to the high Curie temperature, NKN also show large potential for high temperature dielectric capacitors [16,17]. Large W_{rec} values (over 3 − 4 J/cm^3) were reported in NKN-based lead-free ceramics at room temperature after the addition of suitable ABO_3 ($Sr(Zn_{1/3}Nb_{2/3})O_3$, $BiFeO_3$, $SrTiO_3$, $Bi(Mg_{2/3}Nb_{1/3})O_3$ and $Sr(Sc_{0.5}Nb_{0.5})O_3$ and et al.), in which an enhanced electric field can be applied in addition to increased dielectric relaxation degree as a result submicron-scaled grain morphology [18–22]. However, these NKN-based ferroelectric compositions usually exhibit relatively low η, probably owing to large leakage current at high fields as well as defects caused by poor sintering. Nevertheless, the advantage for the high temperature application has rarely been reported for NKN-based energy-storage capacitors. Hence, it will be interesting to further improve energy-storage properties with a special focus on the thermal-stability of energy-storage properties for NKN-based lead-free compositions.

In order to achieve excellent energy storage properties, Li, Sb, Bi $(Zn_{0.5}Zr_{0.5})O_3$ (BZZ) were co-doped into the NKN matrix, where Li and Zn are helpful for the sintering behavior, Sb and Zr tend to stabilize the

* Corresponding author.
E-mail address: piezolab@hfut.edu.cn (R. Zuo).

https://doi.org/10.1016/j.jeurceramsoc.2020.06.048
Received 30 April 2020; Received in revised form 12 June 2020; Accepted 16 June 2020
Available online 20 June 2020
0955-2219/

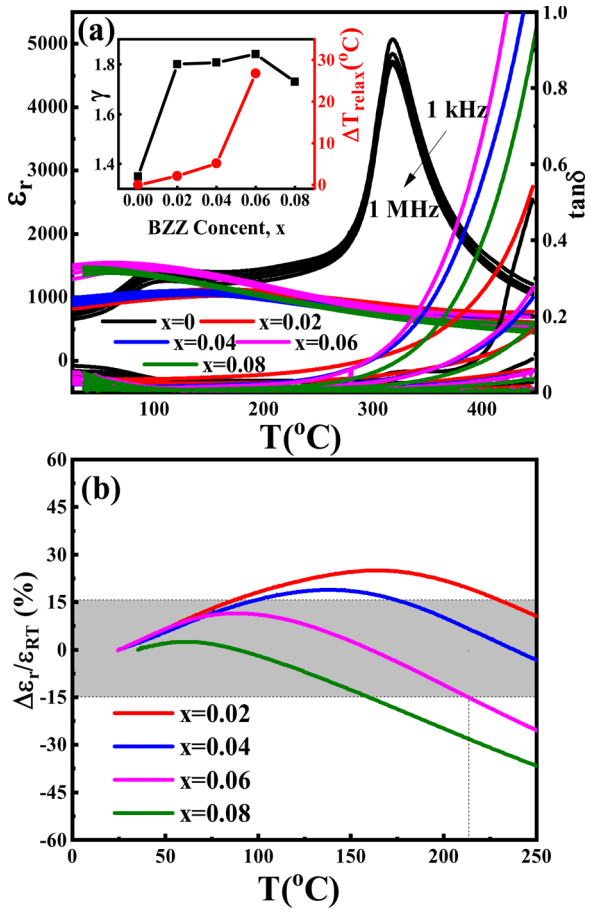

Fig. 1. (a) Dielectric permittivity and loss as a function of temperature and frequency and (b) the temperature dependence of $\Delta\varepsilon_r/\varepsilon_{RT}$ at 1 MHz for NKLNS-*x*BZZ ceramics. The inset in (a) shows the variation of γ and ΔT_{relax} with *x*.

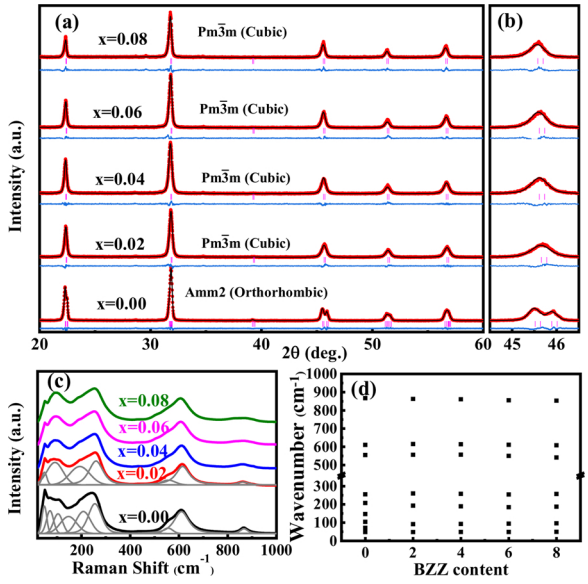

Fig. 2. (a) Room temperature XRD refinements of NKLNS-*x*BZZ ceramics, (b) locally enlarged patterns near $2\theta \sim 46^{\circ}$, (c) Raman spectra at room temperature for the NKLNS-*x*BZZ ceramics and (d) the wavenumber of the observed modes as a function of BZZ content.

low temperature rhombohedral phase and Bi-based perovskites are in favor of the high spontaneous polarization [23–25]. It was reported that doping Sb^{5+} into NKN ceramics can induce an obvious normal FE to relaxor FE phase transition [26]. In addition, the introduction of BZZ can effectively depress the dielectric peak to enhance temperature stability of dielectric permittivity [27]. As a result, $[(Na_{0.5}K_{0.5})_{0.97-x}Li_{0.03}](Nb_{0.94-x}Sb_{0.06})O_3$-$xBi(Zn_{1/2}Zr_{1/2})O_3$ (NKLNS-*x*BZZ) were specially designed, showing obviously improved energy-storage properties.

2. Experimental

The NKLNS-*x*BZZ ($x = 0-0.08$) and NKLNS-0.06BZZ +0.4 wt.% La_2O_3 ceramics were synthesized by a solid-state method using high-purity raw materials : K_2CO_3 (≥99.0 %), Na_2CO_3 (≥99.0 %), Li_2CO_3 (≥99.0 %), Nb_2O_5 (≥99.0 %), Sb_2O_3 (≥99.0 %), ZrO_2 (≥99.0 %), ZnO (≥99.0 %), Bi_2O_3 (≥99.0 %) and La_2O_3 (≥99.0 %). All raw materials were purchased from Sinopharm Chemical Reagent Co., Ltd., CN. The initial materials were dried at 120 °C for 24 h to remove the absorbed moisture. The powders were weighed according to the stoichiometric ratio and mixed in ethanol for 6 h. After drying, the powders were calcined at 850 °C for 4 h. The calcined powers were ball milled again with the dopant, 0.4 wt% La_2O_3 and the binder, 0.6 wt% PVB. Finally, the powders were pressed into disks of 10 mm in diameter and sintered at 1050 − 1150 °C for 2 h. The ceramic samples were polished to obtain parallel surfaces and coated with silver paste and then fired at 550 °C for 30 min.

The phase structures were investigated by an X-ray powder diffractometer (XRD, D/Mzx-rB, Rigaku, Tokyo, Japan) with Cu Kα radiation and Raman spectroscopy (Raman, LabRAM HR Evolution, HORIBA Jobin Yvon, FR). The grain morphology of the samples was observed by a field emission scanning electron microscope (FE-SEM, SU8020, JEOL, Tokyo, Japan). The high-precision LCR meter (Agilent E4980A, Santa Clara, CA) was used to measure the dielectric permittivity and dielectric loss as a function of temperature and frequency and the impedance-frequency spectra. P-E hysteresis loops were measured by a ferroelectric measurement system (Precision multi-ferroelectric, Radiant Technologies Inc, Albuquerque, NM). The dielectric breakdown strength (E_B) was measured by a voltage breakdown tester (BDJC-50 kV, Beijing Beiguang Jingyi Instrument Equipment Co. Ltd, Beijing, CN). The charge-discharge properties of samples were measured using a specially designed and high-speed capacitor discharge circuit.

3. Results and discussion

Fig. 1(a) shows dielectric permittivity and loss as a function of temperature and frequency for NKLNS-*x*BZZ ceramics. Two dielectric anomalies at 80 °C and 320 °C can be observed in the $x = 0$ sample, as observed in pure NKN, corresponding to the orthorhombic-tetragonal and tetragonal-cubic phase transitions, respectively. With the addition of BZZ, only a single diffuse dielectric peak can be found within the measured temperature range. The broadened and suppressed dielectric peak indicates that the normal FE phase at $x = 0$ transforms into a relaxor FE phase ($x \geq 0.02$) at room temperature [28,29]. It is commonly accepted that the dielectric relaxation behavior of relaxor FEs can be defined by a modified Curie-Weiss law: $1/\varepsilon_r - 1/\varepsilon_m = (T-T_m)^{\gamma}/C$ $(T > T_m)$, where γ is the degree of diffusivity, ε_m is the is the maximum value of the dielectric permittivity, T_m is the corresponding temperature at the ε_m, and *C* is the Curie-Weiss constant [30]. Moreover, ΔT_{relax} is also an important parameter to depict dielectric relaxation characteristics, which can be determined by the difference between two T_m values measured at 1 MHz and 1 kHz [31]. Both parameters (γ and ΔT_{relax}) were found to increase obviously with the increase of BZZ content, as shown in the inset of Fig. 1(a), confirming the enhanced dielectric relaxation behavior. This should be related to the introduction of cations with different valences into both A and B sites of the ABO_3 crystal lattice, leading to the increase of the local random field as a result of the disordered distribution of different ions. Moreover, it is worth noting that the improved thermal stability of ε_r can be achieved at the same

Table 1
Refined structural parameters of NKLNS-*x*BZZ ceramics.

x	Space group	a (Å)	b (Å)	c (Å)	Volume (Å^3)	R_{wp} (%)	R_p (%)	χ^2
0	Amm2	3.9533(2)	5.6235(4)	5.6455(3)	125.51	7.72	5.58	1.51
0.02	Pmm	3.9750(2)	3.9750(2)	3.9750(2)	62.81	10.10	7.56	1.19
0.04	Pmm	3.9783(2)	3.9783(2)	3.9783(2)	62.97	9.97	7.41	1.16
0.06	Pmm	3.9827(2)	3.9827(2)	3.9827(2)	63.17	11.64	8.86	1.54
0.08	Pmm	3.9850(2)	3.9850(2)	3.9850(2)	63.29	13.47	10.58	1.43

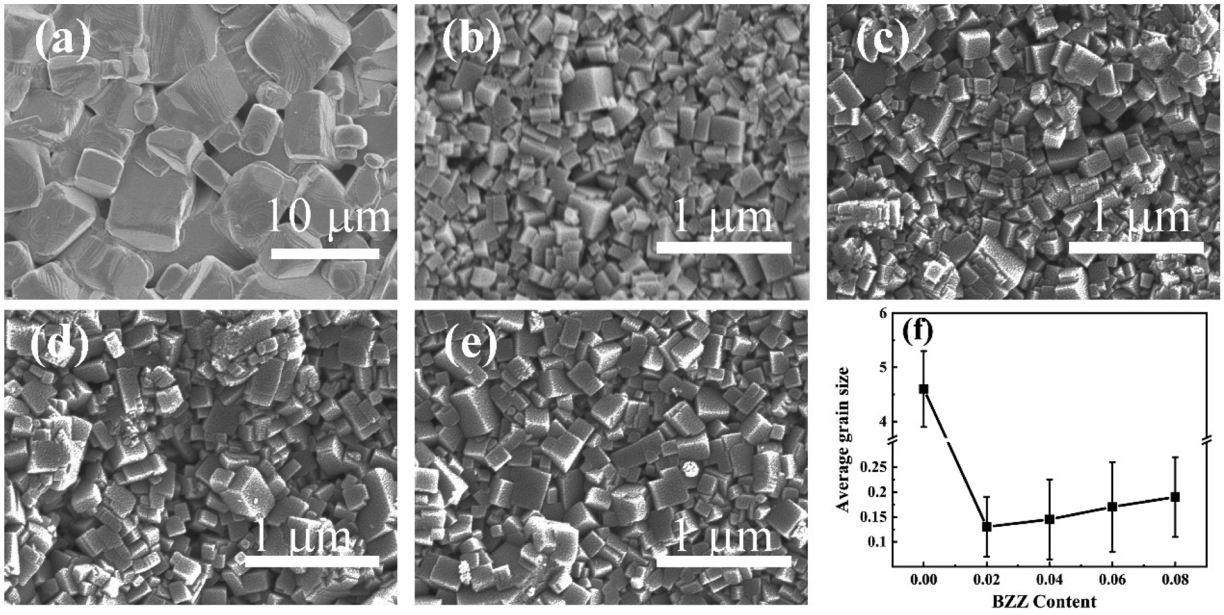

Fig. 3. SEM micrographs of the as-sintered surface of the NKLNS-*x*BZZ ceramics (a) $x = 0$, (b) $x = 0.02$, (c) $x = 0.04$, (d) $x = 0.06$, (d) $x = 0.08$ and (f) the variation of average grain size with increasing BZZ content.

time with the addition of BZZ, as shown in Fig. 1(b). Obviously, the variation of ε_r with temperature doesn't exceed 15 % within the temperature range of 25 ~ 210 °C at 1 MHz in the $x = 0.06$ ceramic, indicating a large potential for temperature-stable dielectric capacitors.

Fig. 2 illustrates the XRD refinement patterns of NKLNS-*x*BZZ ceramics as a function of *x*. It can be seen that all the ceramics exhibit a pure perovskite structure without any impurity phase. To confirm the structural variation of the NKLNS-*x*BZZ ceramics, Rietveld refinement analysis was conducted on the XRD pattern of all specimens using the GSAS software. For the $x = 0$ ceramic, a typical orthorhombic symmetry can be identified, as evidenced by the peak splitting of the (002) and (200) diffraction lines [32]. Therefore, the crystal structure of NKLNS-*x*BZZ ceramics was analyzed using orthorhombic with Amm2 space group. A good fitting profile with $R_{wp} = 7.72$ % and $\chi^2 = 1.51$ indicates a single orthorhombic phase for the $x = 0$ sample. With the addition of BZZ content, the split (200) peaks merge into a single peak, indicating that the NKLNS-*x*BZZ solid solutions undergo a transition from a single orthorhombic phase to a pseudo-cubic phase, as indicated by both single (110) and (200) peaks for the ceramics of $x \geq 0.02$ [33]. Rietveld refinement of NKLNS-*x*BZZ ceramics ($x = 0.02 - 0.08$) was well executed using cubic with Pmm space group [34]. The refined lattice parameters for all ceramics are shown in Table 1. It can be seen that the volume of the perovskite unit cells expands monotonously with increasing BZZ content because of the substitution of larger B-site ions such as Zr^{4+} (0.72 nm, CN = 6) and Zn^{2+} (0.74 nm, CN = 6) for Nb^{5+} (0.64 nm, CN = 6) and Sb^{5+} (0.6 nm, CN = 6) [35,36].

Raman scattering is one of the appropriate techniques to study the dynamics of the local structure by analyzing the characteristic modes associated with nanoregions in relaxor FEs [37]. The Raman scattering spectra and the deconvolution results by using Lorentz function for NKLNS-*x*BZZ ceramics are shown in Figs. 2(c)-(d). For $x = 0$, the peaks at wavenumbers < 150 cm^{-1} are related to the translational modes of Na^+, K^+ and Li^+ cations. The other peaks at about 246 cm^{-1}, 608 cm^{-1} and 860 cm^{-1} are related to the BO_6 octahedra [38]. With the addition of BZZ, the peak at around 246 cm^{-1} becomes weak and broad. The peak around 90 cm^{-1} merges into a single peak after the addition of Bi^{3+} cations into the A site. These indicate that the cation disorder of the A site can be enhanced through the multiple-cation substitution. Moreover, the peaks at around 550 cm^{-1} and 860 cm^{-1} become diffuse and weak slightly with increasing *x*, indicating the increased B-site structural disorder as well after the substitution of Nb^{5+} and Sb^{5+} by $Zr^{4+}$and Zn^{2+}. The simultaneously increased structural disorder at both A and B sites results in the macroscopic dielectric relaxation behavior. After deconvolution by Gaussian-Lorentzian-shape peaks function, the wavenumber of the Raman-active vibrational modes as a function of *x* was shown in Fig. 2(d). It can be seen that 9 Raman peaks were detected for $x = 0$ ceramics while 7 Raman peaks were detected for the ceramics with $x \geq 0.02$. According to the XRD results, this phenomenon should be related to the transformation of the phase structure. Meanwhile, the BO_6 octahedra bands around 608 cm^{-1} and 860 cm^{-1} tend to shift to lower frequency with the addition of BZZ. It means that the increase of BZZ content weakens the interaction between B and O ions and accordingly increases the degree of diffusivity.

Fig. 3(a)-(e) show SEM micrographs of the as-sintered surface of NKLNS-*x*BZZ ceramics at their optimal sintering temperatures and Fig. 3(f) shows the variation of average grain size with increasing BZZ content. The average grain size was estimated by a line-intercept method using Nano Measurer software including 100–120 grains. It can be seen that the grain size for the $x = 0$ ceramic is larger than 4 μm and the microstructure is not dense. With the addition of BZZ, the grain size

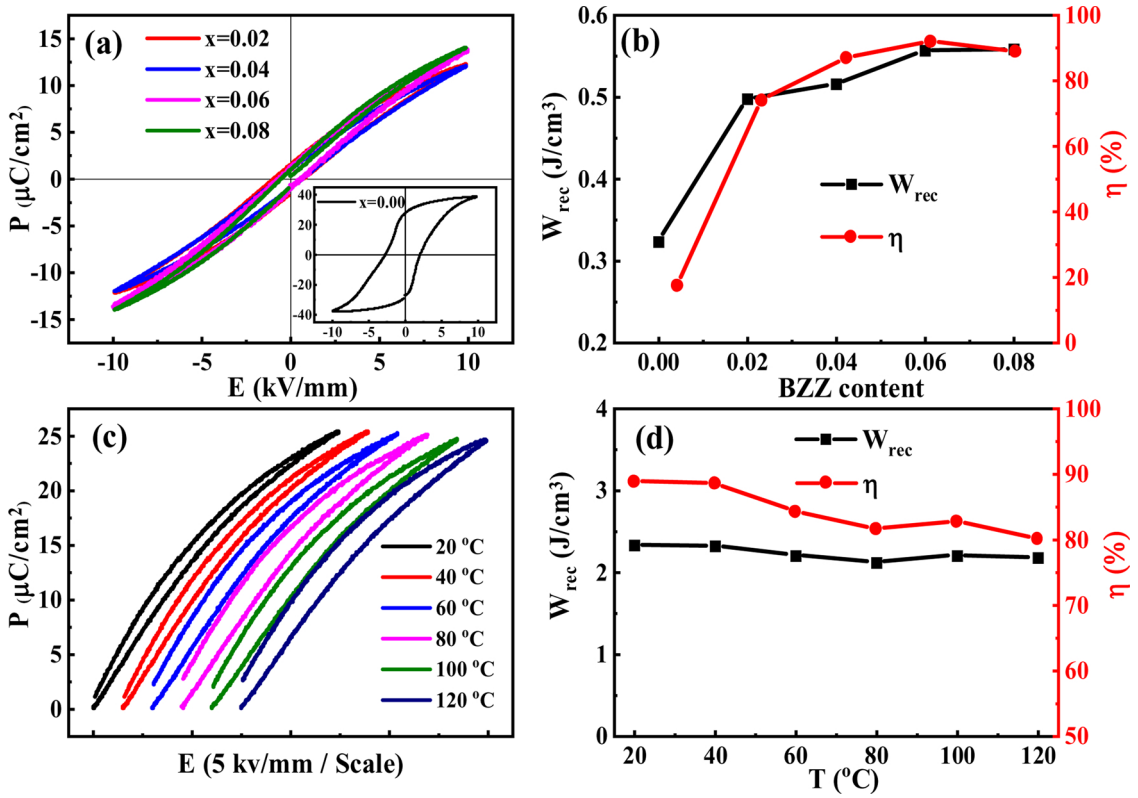

Fig. 4. (a) *P-E* hysteresis loops measured at 100 Hz under 10 kV/mm, (b) the variation of energy-storage performances with increasing BZZ content, (c) the temperature dependence of unipolar *P-E* hysteresis loops of the NKLNS-0.06BZZ ceramic measured at 100 Hz under 25 kV/mm and (d) W_{rec} and η as a function of temperature.

reduces down to submicron scales. In addition, the average grain size increases gradually for $x \geq 0.02$ because the existence of Zn can produce liquid phases and thus promote grain growth [24].

Fig. 4(a) shows *P-E* hysteresis loops of NKLNS-*x*BZZ ceramics under 10 kV/mm. The $x = 0$ ceramic exhibits a square-like *P-E* loop with relatively large P_{max} and P_r, typical of a normal FE characteristic. After the addition of BZZ, slim P-E loops with small P_r values can be observed. Fig. 4(b) shows the variation of energy-storage performances under 10 kV/mm with changing BZZ content. Accompanying the transition from normal FE phase to relaxor FE phase, the values of η and W_{rec} increase rapidly from $x = 0$ to $x = 0.02$. With further enhancing dielectric relaxation degree, both η and W_{rec} increase tardily. Maximum ΔP ($=P_{max}$-P_r) value ($\approx$15 μC/cm^2) was obtained at $x = 0.06$, laying a good foundation for achieving the optimum W_{rec} value of ~0.6 J/cm^3. Moreover, the $x = 0.06$ ceramic also exhibits a relatively high η value of ~92 %, meaning that only a small part of the charging energy can be dissipated as heat during the discharge process. To explore the temperature dependence of energy-storage performance, unipolar *P-E* hysteresis loops for NKLNS-0.06BZZ ceramics under 25 kV/mm at different temperature are shown in Fig. 4(c). Slim P-E hysteresis loops with small P_r and large P_{max} can be seen in the studied temperature range. W_{rec} decreases slightly from 2.3 J/cm^3 to 2.1 J/cm^3 while η decreases from 89 % to 78 % on heating, as shown in Fig. 4(d). The reason for the decrease in η is probably attributed to the increase in oxygen vacancy concentration at high temperatures.

To further improve the energy-storage performance of the $x = 0.06$ ceramic, 0.4 wt.% La_2O_3 was added for the purposed to optimize grain morphology and thus increase E_B [39]. Fig. 5(a) and (b) show SEM micrographs of the as-sintered surface of undoped and doped NKLNS-0.06BZZ ceramics at their optimal temperatures, respectively. It can be seen that both samples exhibit compact microstructure. The distribution of grain size is shown in the insets of Fig. 5(a) and (b). The distribution of grain size was fitted by Gauss formula using Origin software. Although a few larger grains exist in doped samples, the doped samples have smaller average grain sizes and more uniform grains. Considering the similarity of ionic radius between K^+, Na^+ and La^{3+}, La^{3+} can easily diffuse into the crystal lattice occupying the A-site in NKN-based ceramics [40]. Point defects may exist in the ABO_3 crystal structure after doping La^{3+}, as described by the following reaction: $La_2O_3 \xrightarrow{A^+B^{5+}O_3} 2La_A^{\cdot} + 3O_O + 4V_A^{'}$ [41]. The generated A-site vacancies or electrons can combine with oxygen vacancies, forming defect dipoles, leading to the reduction in the content of independent oxygen vacancies. Furthermore, grain growth can be inhibited as a result of the pinning of the movement of grain boundary during sintering process after adding La_2O_3 [16]. Temperature-dependent dielectric permittivity of undoped and doped samples is shown in Fig. 5(c). T_m keeps nearly unchanged, while the maximum dielectric permittivity slightly decreases with the addition of La_2O_3 probably because of the grain refinement. The dielectric loss tanδ of La_2O_3 doped samples is lower than that of undoped samples, especially at high temperature. Fig. 5(d) shows the complex impedance plane Z'-Z" plot of undoped and doped NKLNS-0.06BZZ ceramics measured at 500 °C. The electric conductivity mechanism can be obtained from the impedance spectra. Generally speaking, grain and grain boundary affect the electrical process corresponding to two *Debye*-like semicircles shown in the impedance spectra. According to the fitting results using an equivalent circuit shown in Fig. 5(d), the grain boundary is believed to make the main contribution to the electrical process [42,43]. In addition, the increase of grain boundary resistivity indicates that doping La_2O_3 can efficiently enhance the insulation behavior of NKLNS-0.06BZZ ceramics. Fig. 5(e) illustrates the dielectric loss tanδ at room temperature as a function of frequency for undoped and doped NKLNS-0.06BZZ ceramics. It can be seen that tanδ for both samples increases with increasing frequency. The increase in tanδ should be caused by the dielectric relaxation at higher frequency. For the doped NKLNS-0.06BZZ ceramic,

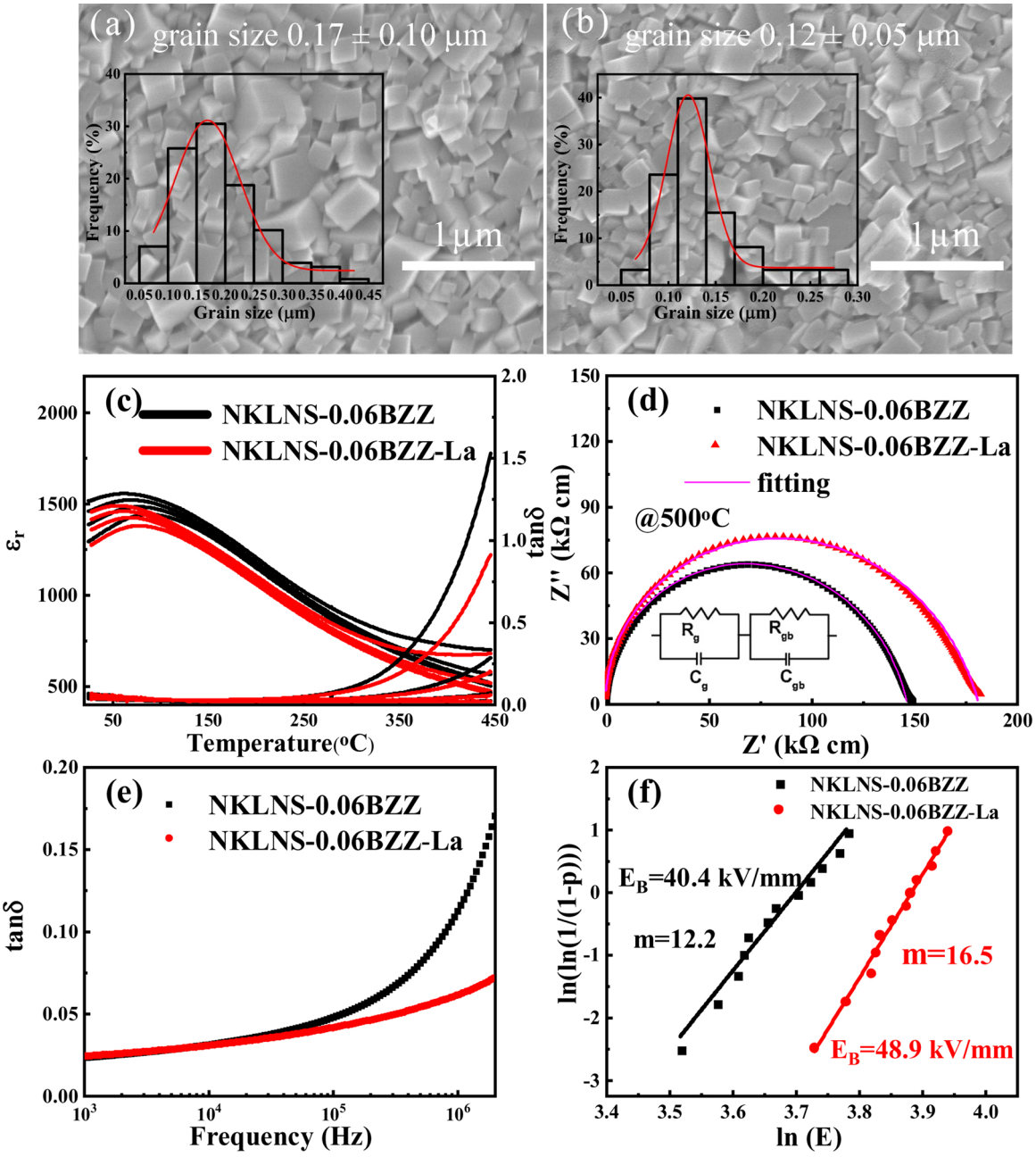

Fig. 5. SEM micrographs of the as-sintered surface of (a) NKLNS-0.06BZZ and (b) La_2O_3 doped NKLNS-0.06BZZ ceramics, (c) temperature dependent dielectric permittivity, (d) the complex impedance plane *Z'-Z''* plot measured at 500 °C, (e) dielectric loss tanδ as a function of frequency at room temperature and (f) the *Weibull* statistical distribution of undoped and doped NKLNS-0.06BZZ ceramics.

the tanδ is lower than that of the undoped ceramic over the measured frequency range, especially at higher frequency. An important reason for the reduction of tanδ is the increase of the fraction of grain boundary with larger resistivity. When an electric field is applied, heat will be continuously generated within the dielectric because of the conductive leakage current and/or dielectric loss. The decreased dielectric loss would decrease the possibility of thermal breakdown and thus increase E_B of bulk ceramics after adding La_2O_3. In order to quantitatively evaluate the E_B value of the two ceramics, the *Weibull* statistical distribution method [44–46] was used, as shown in Fig. 5(f), according to the following equations: $X_i = ln(E_i)$, $Y_i = ln\,(ln(1/(1-P_i)))$, $P_i = i/(n+1)$ where X_i, Y_i, and P_i are parameters in Weibull distribution functions, n is the total number of samples, and E_i is the breakdown electric field of each sample in the experiments. E_i should be arranged in ascending order of electric field. The result of the linear regression fit can be expressed as $Y = A + mX$, where m is the Weibull parameter. It is greater than 11, indicating that the analysis result is credible. As a result, E_B values of undoped and doped NKLNS-0.06BZZ ceramics are 41.6 kV/mm and 48.9 kV/mm, respectively. The improved E_B should be ascribed to the combined contribution of decreased grain size, increased bulk resistivity and decreased dielectric loss caused by La_2O_3 doping.

Large E_B values allow high electric fields to be applied. Fig. 6(a) shows unipolar *P-E* hysteresis loops of undoped and doped NKLNS-0.06BZZ ceramics under different electric fields. With increasing electric field, P_{max} increases while P_r remains very small, leading to an obvious increase of ΔP, as shown in Fig. 6(b). P_{max} of the undoped NKLNS-0.06BZZ ceramic increases from ~13.9 at 10 kV/mm to ~30.9 μC/cm^2 at 38 kV/mm, while P_{max} of the La_2O_3 doped NKLNS-0.06BZZ ceramic increases from ~12.7 at 10 kV/mm to ~31.5 μC/cm^2 at 48

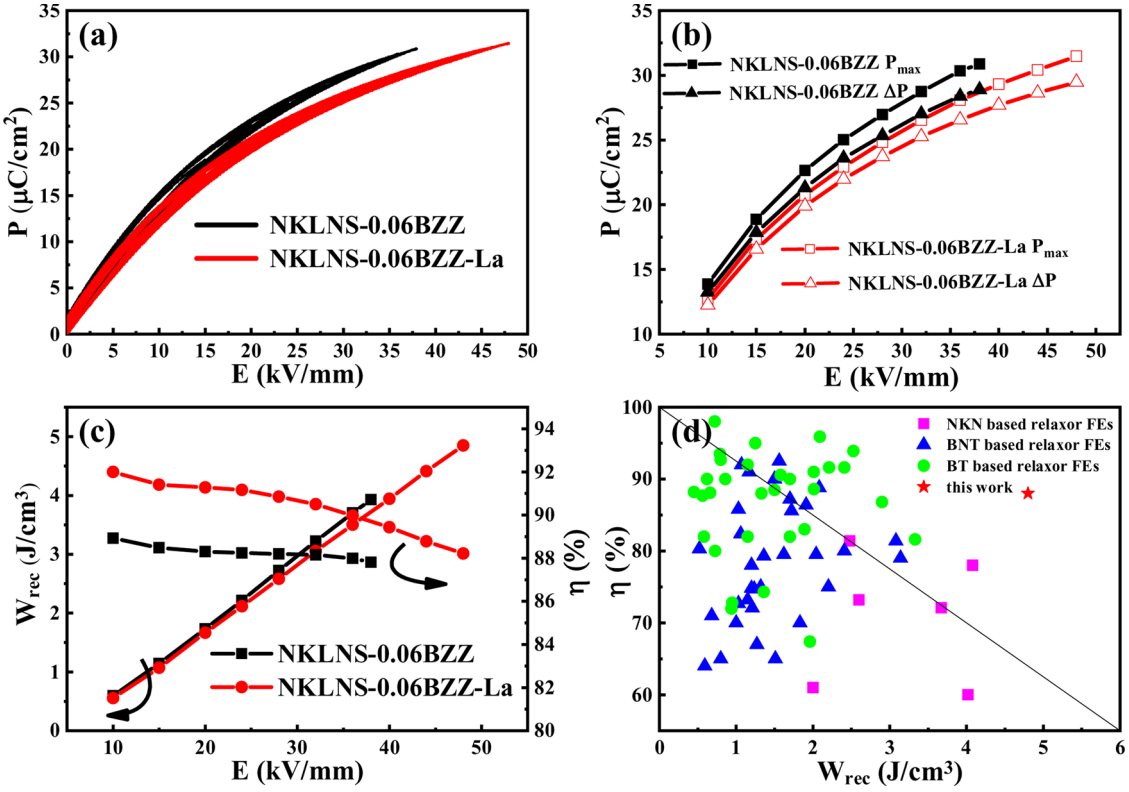

Fig. 6. (a) Unipolar *P-E* hysteresis loops at 100 Hz measured at room temperature, (b) P_{max} and ΔP (c) W_{rec} and η as a function of electric field for undoped and doped NKLNS-0.06BZZ ceramics and (d) energy-storage properties of the La_2O_3 doped NKLNS-0.06BZZ sample and some other lead-free ceramics [1,18–22,47–51].

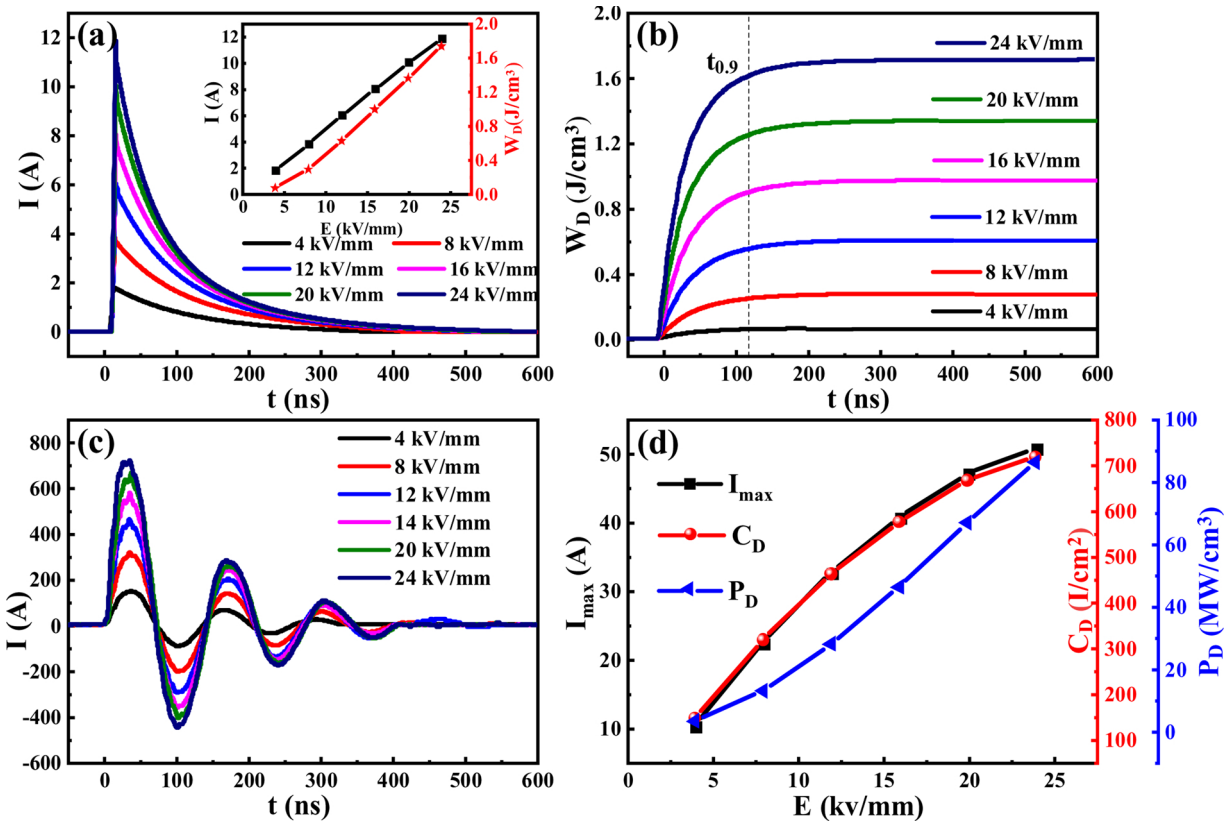

Fig. 7. (a) Pulsed overdamped discharge current curves of the La_2O_3 doped NKLNS-0.06BZZ ceramic under various electric fields. The inset shows maximum current (I_{max}), and discharge energy density (W_D) as a function of electric fields, (b) W_D as a function of time for the NKLNS-0.06BZZ ceramic measured under various electric fields, (c) underdamped discharge waveforms for the NKLNS-0.06BZZ ceramic measured under different electric fields, and (d) the variation of I_{max}, current density ($C_D = I_{max}/S$) and power density ($P_D = EI_{max}/2S$, where S and E mean the electrode area of the sample and the electric field strength, respectively) with changing electric field.

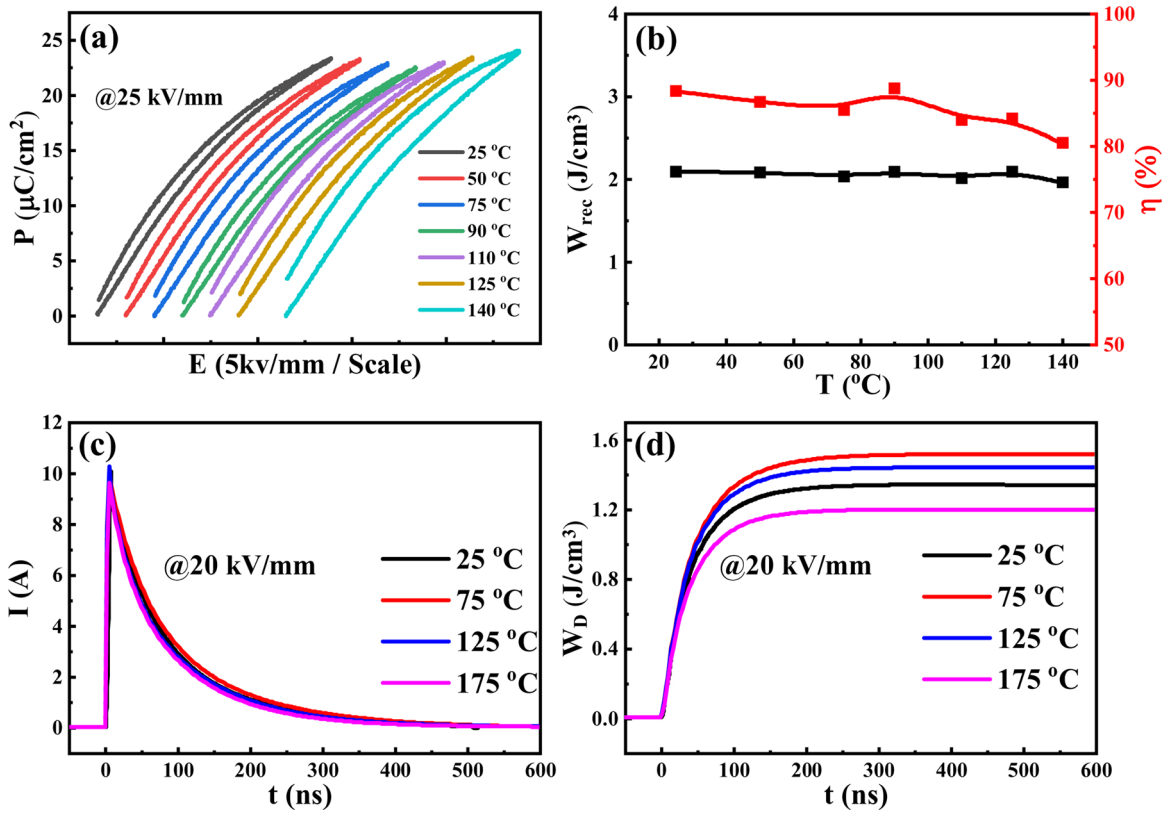

Fig. 8. (a) The temperature dependence of unipolar *P-E* hysteresis loops of the La_2O_3 doped NKLNS-0.06BZZ ceramic measured at 100 Hz under 25 kV/mm, (b) W_{rec} and η as a function of temperature, (c) temperature dependence of the pulsed overdamped discharge current curves of the La_2O_3 doped NKLNS-0.06BZZ ceramic under 20 kV/mm and (d) W_D as a function of time at different temperatures.

kV/mm. Large W_{rec} of 3.93 J/cm^3 and 4.85 J/cm^3 were obtained in undoped and doped NKLNS-0.06BZZ ceramics, respectively, under their respective testable electric fields, as shown in Fig. 6(c). In addition, the energy-storage efficiency of undoped and doped NKLNS-0.06BZZ ceramics under different electric fields is also shown in Fig. 6(c). It can be seen that η slightly decreases with increasing electric fields. Within the applied electric field range, η values of the doped NKLNS-0.06BZZ ceramic are always higher than those of the undoped ceramic. The reason may be that the leakage current caused by electric field is reduced after doping La_2O_3. A large η ~88.2 % was obtained for La_2O_3 doped NKLNS-0.06BZZ ceramic under 48 kV/mm. Fig. 6(d) compares the energy storage properties of the NKLNS-0.06BZZ ceramics with a few other lead-free ceramic samples. As can be seen, there is an obvious relationship of the mutual constraint between W_{rec} and η for these lead-free ceramics. W_{rec} and η are commonly located under the diagonal of Fig. 6(d). For $(Bi_{0.5}Na_{0.5})TiO_3$ (BNT) based and $BaTiO_3$ (BT) based relaxor FEs, large η (~90 %) can be obtained while W_{rec} is usually less than 3 J/cm^3. For NKN based ceramics, η is usually less than 80 %. By comparison, large W_{rec} and η can be obtained simultaneously in the studied sample, showing obvious advantages for future energy-storage capacitors.

The actual charging-discharging characteristic is one of the most important factors for applications in pulsed power systems. Fig. 7(a) shows the electric field dependence of overdamped pulsed discharge electric current-time (*I-t*) curves of the La_2O_3 doped NKLNS-0.06BZZ ceramic. It is clear that the current reaches the maximum value in a very short time under different electric fields. The W_D shown in Fig. 7(b) can be calculated using $W_D = R\int I(t)dt/V$, where R of the total loading resistor is 200 Ω and V is the volume of the sample [52,53]. The I_{max} and the maximum W_D rise from 1.81 A and 0.073 J/cm^3 to 11.86 A and 1.74 J/cm^3, respectively, with the electric field raising from 4 kV/mm to 24 kV/mm. The value of $t_{0.9}$ reflects the discharge speed, which describes the time to release 90 % of the stored energy. The value of $t_{0.9}$ is about 112 ns, which is smaller than that of some other reported relaxor FEs [13,54]. Fig. 7(c) shows underdamped discharge waveforms under different electric fields, displaying similar discharge performances [55]. It is clear that all discharging currents have the same tendency and the first current peak increases with increasing electric field. Fig. 7(d) illustrates the change of I_{max}, C_D, and P_D. The I_{max} values increase from 10.2 A to 50.6 A, while C_D and P_D increase from 144 A/cm^2 and 2.9 MW/cm^3 to 716 A/cm^2 and 86.0 MW/cm^3, respectively. High values of I_{max} (~50.6 A), C_D (~716 A/cm^2) and P_D (~86.0 MW/cm^3) in the doped NKLNS-0.06BZZ ceramic were obtained under 24 kV/mm, indicating an ideal candidate for pulsed power applications.

For ceramic capacitors, good thermal-stability of energy-storage performance is also an important parameter. The temperature dependence of unipolar *P-E* hysteresis loops for La_2O_3 doped NKLNS-0.06BZZ ceramics measured under 25 kV/mm is shown in Fig. 8(a). Slim *P-E* hysteresis loops with small P_r can be seen in the studied temperature range, while the values of P_{max} are relatively stable between 22.6 μC/cm^2 and 24.5 μC/cm^2. As a result, W_{rec} keeps almost unchanged (~ 2 J/cm^3) and η remains ≥ 80 % on heating, as shown in Fig. 8(b). In the temperature range of 25–140 °C, W_{rec} and η vary with changing temperature within 12 %, indicating that La_2O_3 doped NKLNS-0.06BZZ ceramics exhibit a good temperature stability. Figs. 8(c)-(d) show the temperature dependence of *I-t* curves and W_D-*t* curves measured under 20 kV/mm. It is clear that I_{max} remains approximately 10 A within the measured temperature range of 25–175 °C. Meanwhile, W_D firstly increases slightly and then decreases, because of the change of dielectric permittivity with increasing temperature. Nevertheless, W_D can remain in the range of 1.19 J/cm^3 ~ 1.34 J/cm^3 from room temperature to 175 °C. At the same time, small $t_{0.9}$ values between 100 and 114 ns can be detected in the studied temperature range, suggesting a very fast discharge speed. Temperature-stable energy storage properties in the

studied sample would provide guarantees for applications over a wide temperature range.

4. Conclusions

Lead-free NKLNS-*x*BZZ relaxor FE ceramics were investigated for pulsed power applications in this work. With increasing BZZ content, the ceramics transform from a normal FE phase into a relaxor FE phase. Optimal energy-storage performances (W_{rec} ~ 3.93 J/cm^3 and η ~ 87.7 %) were obtained in the x = 0.06 ceramic under 38 kV/mm. To further improve the energy-storage performance, 0.4 wt.% La_2O_3 was introduced to enhance the breakdown strength through reducing grain size, decreasing dielectric loss and enhancing bulk resistivity. As a result, a high W_{rec} of 4.85 J/cm^3 and a large η of 88.2 % were obtained at the same time under 48 kV/mm at room temperature. Meanwhile, the La_2O_3-doped NKLNS-0.06BZZ ceramic exhibits a good thermal stability of energy-storage properties in the temperature range of 25 ~ 140 °C due to the diffuse phase transition on heating. The charge-discharge properties of W_D = 1.74 J/cm^3, I_{max} = 11.86 A and $t_{0.9}$ = 112 ns under 24 kV/mm are advantageous for the energy storage applications. The temperature-stable energy-storage properties and excellent charge-discharge characteristics should make the La_2O_3-doped NKLNS-0.06BZZ ceramic become an attractive candidate for future dielectric capacitors which require ideal thermal stability.

Declaration of Competing Interest

The authors declare that they have no known competing financial interests or personal relationships that could have appeared to influence the work reported in this paper.

Acknowledgements

This work was financially supported by the National Natural Science Foundation of China (Grant no. U19A2087 and U1432113). Thank Dr. He Qi and Dr. Aiwen Xie for valuable helps in the data measurement and discussion.

References

[1] L.T. Yang, X. Kong, F. Li, H. Hao, Z.X. Cheng, H.X. Liu, J.F. Li, S.J. Zhang, Perovskite lead-free dielectrics for energy storage applications, Prog. Mater. Sci. 102 (2019) 72–108.
[2] K.L. Zou, Y. Dan, H.J. Xu, Q.F. Zhang, Y.M. Lu, H.T. Huang, Y.B. He, Recent advances in lead-free dielectric materials for energy storage, Mater. Res. Bull. 113 (2019) 190–201.
[3] X.H. Hao, A review on the dielectric materials for high energy-storage application, J. Adv. Dielectr. 3 (1) (2013) 1330001.
[4] Y.H. Huang, Y.J. Wu, W.J. Qiu, J. Li, X.M. Chen, Enhanced energy storage density of $Ba_{0.4}Sr_{0.6}TiO_3$-MgO composite prepared by spark plasma sintering, J. Eur. Ceram. Soc. 35 (5) (2015) 1469–1476.
[5] S. Kwon, W. Hackenberger, E. Alberta, E. Furman, M. Lanagan, Nonlinear dielectric ceramics and their applications to capacitors and tunable dielectrics, IEEE Electr Insul M 27 (2) (2011) 43–55.
[6] N.N. Luo, K. Han, F.P. Zhuo, C. Xu, G.Z. Zhang, L.J. Liu, X.Y. Chen, C.Z. Hu, H.F. Zhou, Y.Z. Wei, Aliovalent A-site engineered $AgNbO_3$ lead-free antiferroelectric ceramics toward superior energy storage density, J. Mater. Chem. A Mater. Energy Sustain. 7 (23) (2019) 14118–14128.
[7] T. Wang, L. Jin, C.C. Li, Q.Y. Hu, X.Y. Wei, Relaxor ferroelectric $BaTiO_3$-$Bi(Mg_{2/3}Nb_{1/3})O_3$ ceramics for energy storage application, J. Am. Ceram. Soc. 98 (2) (2015) 559–566.
[8] B.C. Luo, X.H. Wang, E.K. Tian, H.Z. Song, H.X. Wang, L.T. Li, Enhanced energy-storage density and high efficiency of lead-free $CaTiO_3$-$BiScO_3$ linear dielectric ceramics, ACS Appl. Mater. Interfaces 9 (23) (2017) 19963–19972.
[9] H. Qi, R.Z. Zuo, Linear-like lead-free relaxor antiferroelectric $(Bi_{0.5}Na_{0.5})TiO_3$-$NaNbO_3$ with giant energy-storage density/efficiency and super stability against temperature and frequency, J. Mater. Chem. A Mater. Energy Sustain. 7 (8) (2019) 3971–3978.
[10] H. Borkar, V.N. Singh, B.P. Singh, M. Tomar, V. Gupta, A. Kumar, Room temperature lead-free relaxor-antiferroelectric electroceramics for energy storage applications, RSC Adv. 4 (44) (2014) 22840–22847.
[11] D.G. Zheng, R.Z. Zuo, Enhanced energy storage properties in $La(Mg_{1/2}Ti_{1/2})O_3$-modified $BiFeO_3$-$BaTiO_3$ lead-free relaxor ferroelectric ceramics within a wide temperature range, J. Eur. Ceram. Soc. 37 (1) (2017) 413–418.
[12] N.N. Sun, Y. Li, Q.W. Zhang, X.H. Hao, Giant energy-storage density and high efficiency achieved in $(Bi_{0.5}Na_{0.5})TiO_3$-$Bi(Ni_{0.5}Zr_{0.5})O_3$ thick films with polar nanoregions, J. Mater. Chem. C Mater. Opt. Electron. Devices 6 (40) (2018) 10693–10703.
[13] M.X. Zhou, R.H. Liang, Z.Y. Zhou, X.L. Dong, Novel $BaTiO_3$-based lead-free ceramic capacitors featuring high energy storage density, high power density, and excellent stability, J. Mater. Chem. C Mater. Opt. Electron. Devices 6 (31) (2018) 8528–8537.
[14] K. Wang, J.F. Li, (K, Na)NbO_3-based lead-free piezoceramics: phase transition, sintering and property enhancement, J. Adv. Ceram. 1 (1) (2012) 24–37.
[15] J.G. Wu, D.Q. Xiao, J.G. Zhu, Potassium-sodium niobate lead-free piezoelectric materials: past, present, and future of phase boundaries, Chem. Rev. 115 (7) (2015) 2559–2595.
[16] D.J. Gao, K.W. Kwok, D.M. Lin, H.L.W. Chan, Microstructure and electrical properties of La-modified $K_{0.5}Na_{0.5}NbO_3$ lead-free piezoelectric ceramics, J. Phys. D Appl. Phys. 42 (3) (2009) 035411–035417.
[17] H.L. Cheng, H.L. Du, W.C. Zhou, D.M. Zhu, F. Luo, B. Xu, $Bi(Zn_{2/3}Nb_{1/3})O_3$-$(K_{0.5}Na_{0.5})NbO_3$ high-temperature lead-free ferroelectric ceramics with low capacitance variation in a broad temperature usage range, J. Am. Ceram. Soc. 96 (3) (2013) 833–837.
[18] B.Y. Qu, H.L. Du, Z.T. Yang, Lead-free relaxor ferroelectric ceramics with high optical transparency and energy storage ability, J. Mater. Chem. C Mater. Opt. Electron. Devices 4 (9) (2016) 1795–1803.
[19] Z.T. Yang, H.L. Du, S.B. Qu, Y.D. Hou, H. Ma, J.F. Wang, J. Wang, X.Y. Wei, Z. Xu, Significantly enhanced recoverable energy storage density in potassium-sodium niobate-based lead free ceramics, J. Mater. Chem. A Mater. Energy Sustain. 4 (36) (2016) 13778–13785.
[20] T.Q. Shao, H.L. Du, H. Ma, S.B. Qu, J. Wang, J.F. Wang, X.Y. Wei, Z. Xu, Potassium-sodium niobate based lead-free ceramics: novel electrical energy storage materials, J. Mater. Chem. A Mater. Energy Sustain. 5 (2) (2017) 554–563.
[21] Q.Z. Chai, D. Yang, X.M. Zhao, X.L. Chao, Z.P. Yang, Lead-free \(K.,Na)NbO_3-based ceramics with high optical transparency and large energy storage ability, J. Am. Ceram. Soc. 101 (6) (2018) 2321–2329.
[22] Z.T. Yang, F. Gao, H.L. Du, L. Jin, L.L. Yan, Q.Y. Hu, Y. Yu, S.B. Qu, X.Y. Wei, Z. Xu, Y.J. Wang, Grain size engineered lead-free ceramics with both large energy storage density and ultrahigh mechanical properties, Nano Energy 58 (2019) 768–777.
[23] Rz. Zuo, J. Fu, Dy. Lv, Y. Liu, Antimony tuned rhombohedral-orthorhombic phase transition and enhanced piezoelectric properties in sodium potassium niobate, J. Am. Ceram. Soc. 93 (9) (2010) 2783–2787.
[24] H.T. Li, B.P. Zhang, M. Cui, W.G. Yang, N. Ma, J.F. Li, Microstructure, crystalline phase, and electrical properties of ZnO added $Li_{0.06}(Na_{0.535}K_{0.48})_{0.94}NbO_3$ ceramics, Curr. Appl. Phys. 11 (3) (2011) S184–S188.
[25] G.Z. Zang, Y. Wang, X.J. Yi, J. Du, Z.J. Xu, Effect of Li on the microstructure and electrical properties of $(K_{0.17}Na_{0.83})NbO_3$ lead-free piezoceramics, Curr. Appl. Phys. 11 (2) (2011) 223–226.
[26] J. Fu, R.Z. Zuo, H. Qi, C. Zhang, J.F. Li, L.T. Li, Low electric-field driven ultrahigh electrostrains in Sb-substituted (Na,K)NbO_3 lead-free ferroelectric ceramics, Appl. Phys. Lett. 105 (24) (2014) 092904.
[27] X.L. Chen, D.D. Ma, G.S. Huang, J. Chen, H.F. Zhou, L. Fang, $(K_{0.5}Na_{0.5})NbO_3$-$Bi(Zn_{0.5}Zr_{0.5})O_3$ perovskite ceramics: high relative permittivity, low dielectric loss and good thermal stability, Ceram. Int. 41 (10) (2015) 13883–13886.
[28] G.C. Deng, G.R. Li, A.L. Ding, Q.R. Yin, Evidence for oxygen vacancy inducing spontaneous normal-relaxor transition in complex perovskite ferroelectrics, Appl. Phys. Lett. 87 (19) (2005) 192905.
[29] Z.Y. Liu, H.Q. Fan, C.B. Long, Dielectric nonlinearity and electrical properties of $K_{0.5}Na_{0.5}NbO_3$-$SrTiO_3$ relaxor ferroelectrics, J. Mater. Sci. 49 (23) (2014) 8107–8115.
[30] A. Dixit, S.B. Majumder, R.S. Katiyar, A.S. Bhalla, Relaxor behavior in sol-gel-derived $BaZr_{0.40}Ti_{0.60}O_3$ thin films, Appl. Phys. Lett. 82 (16) (2003) 2679–2681.
[31] P. Mahesh, S. Thota, D. Pamu, Dielectric response and AC-conductivity studies of Gd_2O_3-contained $K_{0.5}Na_{0.5}NbO_3$ piezoelectric ceramics, IEEE Trans. Dielectr. Electr. Insul. 22 (6) (2015) 3668–3675.
[32] D.M. Lin, K.W. Kwok, K.H. Lam, H.L.W. Chan, Structure, piezoelectric and ferroelectric properties of Li- and Sb-modified $K_{0.5}Na_{0.5}NbO_3$ lead-free ceramics, J. Phys. D Appl. Phys. 40 (11) (2007) 3500–3505.
[33] J. Du, J.F. Wang, G.Z. Zang, X.J. Yi, Phase transition behavior and piezoelectric properties of low-Li and high-Sb modified KNN based piezoceramics, Phys. B (Amsterdam, Neth.) 406 (21) (2011) 4077–4079.
[34] D.H. Kim, T.G. Lee, S.H. Cho, K.T. Lee, T.H. Lee, Y.W. Hong, C.H. Hong, J.S. Kim, S. Nahm, Piezoelectric properties of $(Na_{0.5}K_{0.5})(Nb_{1-x}Sb_x)O_3$-$SrTiO_3$ ceramics with tetragonal-pseudocubic PPB structure, J. Am. Ceram. Soc. 101 (9) (2018) 3997–4010.
[35] Y. Huan, X.H. Wang, T. Wei, P.Y. Zhao, J. Xie, Z.F. Ye, L.T. Li, Defect control for enhanced piezoelectric properties in SnO_2 and ZrO_2 co-modified KNN ceramics fired under reducing atmosphere, J. Eur. Ceram. Soc. 37 (5) (2017) 2057–2065.
[36] M.R. Varma, R. Raghunandan, M.T. Sebastian, Effect of dopants on microwave dielectric properties of $Ba(Zn_{1/3}Ta_{2/3})O_3$ ceramics, J. Appl. Phys. 44 (Part 1 (1A)) (2005) 298–303.
[37] L. Zhang, Y.P. Pu, M. Chen, T.C. Wei, W. Keipper, R. Shi, X. Guo, R. Li, X. Peng, High energy-storage density under low electric fields and improved optical transparency in novel sodium bismuth titanate-based lead-free ceramics, J. Eur. Ceram. Soc. 40 (1) (2020) 71–77.
[38] K. Kakimoto, K. Akao, Y.P. Guo, H. Ohsato, Raman scattering study of piezoelectric $(Na_{0.5}K_{0.5})NbO_3$-$LiNbO_3$ ceramics, J. Appl. Phys. 44 (Part 1 (9B)) (2005) 7064–7067.
[39] Q.C. Zhao, X.H. Wang, H.L. Gong, B.B. Liu, B.C. Luo, L.T. Li, The properties of Al_2O_3

coated fine-grain temperature stable $BaTiO_3$-based ceramics sintered in reducing atmosphere, J. Am. Ceram. Soc. 101 (3) (2018) 1245–1254.
[40] Y.J. Zhao, L.H. Wang, R. Huang X, R.Z. Liu, H.P. Zhou, The correlation between the microstructure and macroscopic properties of (K,Na,Li)(Nb,Ta)O_3 ceramic via rare earth oxide doping, Ceram. Int. 40 (1) (2014) 2505–2510.
[41] W.J. Wu, J. Li, D.Q. Xiao, M. Chen, Y.C. Ding, C.Q. Liu, Defect dipoles-driven ferroelectric behavior in potassium sodium niobate ceramics, Ceram. Int. 40 (8) (2014) 13205–13210.
[42] X.Z. Deng, L.Y. Zhang, X.Y. Geng, J. Zhang, L. Sun, R.X. Wang, Z.B. Gu, S.T. Zhang, Crystal structure, impedance, and multiferroic property of $SrZrO_3$ and MnO_2 modified 0.725$BiFeO_3$-0.275$BaTiO_3$ ceramics, Ceram. Int. 43 (17) (2017) 14748–14755.
[43] X.L. Chao, X.D. Ren, X.S. Zhang, Z.H. Peng, J.J. Wang, P.F. Liang, D. Wu, Z.P. Yang, Excellent optical transparency of potassium-sodium niobate-based lead-free relaxor ceramics induced by fine grains, J. Eur. Ceram. Soc. 39 (13) (2019) 3684–3692.
[44] J.J. Huang, Y. Zhang, T. Ma, H.T. Li, L.W. Zhang, Correlation between dielectric breakdown strength and interface polarization in barium strontium titanate glass ceramics, Appl. Phys. Lett. 96 (4) (2010) 042902.
[45] B.B. Liu, X.H. Wang, R.X. Zhang, L.T. Li, Grain size effect and microstructure influence on the energy storage properties of fine-grained $BaTiO_3$-based ceramics, J. Am. Ceram. Soc. 100 (8) (2017) 3599–3607.
[46] X. Kong, L.T. Yang, Z.X. Cheng, S.J. Zhang, Bi-modified $SrTiO_3$-based ceramics for high-temperature energy storage applications, J. Am. Ceram. Soc. 103 (3) (2020) 1722–1731.
[47] B.Y. Qu, H.L. Du, Z.T. Yang, Q.H. Liu, T.H. Liu, Enhanced dielectric breakdown strength and energy storage density in lead-free relaxor ferroelectric ceramics prepared using transition liquid phase sintering, RSC Adv. 6 (41) (2016) 34381–34389.
[48] F. Si, B. Tang, Z.X. Fang, H. Li, S.R. Zhang, Enhanced energy storage and fast charge-discharge properties of (1-x)$BaTiO_3$-x$Bi(Ni_{1/2}Sn_{1/2})O_3$ relaxor ferroelectric ceramics, Ceram. Int. 45 (14) (2019) 17580–17590.
[49] J.B. Wang, H.Q. Fan, B. Hu, H. Jiang, Enhanced energy-storage performance and temperature-stable dielectric properties of (1-x)(0.94$Na_{0.5}Bi_{0.5}TiO_3$-0.06$BaTiO_3$)-x$Na_{0.73}Bi_{0.09}NbO_3$ ceramics, J. Mater. Sci.: Mater. Electron. 30 (3) (2019) 2479–2488.
[50] M.X. Zhou, R.H. Liang, Z.Y. Zhou, X.L. Dong, Combining high energy efficiency and fast charge-discharge capability in novel $BaTiO_3$-based relaxor ferroelectric ceramic for energy-storage, Ceram. Int. 45 (3) (2019) 3582–3590.
[51] H. Qi, A.W. Xie, A. Tian, R.Z. Zuo, Superior energy-storage capacitors with simultaneously giant energy density and efficiency using nanodomain engineered $BiFeO_3$-$BaTiO_3$-$NaNbO_3$ lead-free bulk ferroelectrics, Adv. Energy Mater. 10 (6) (2020) 1903338.
[52] Z.K. Xie, B. Peng, S.Q. Meng, Y.Y. Zhou, Z.X. Yue, High-energy-storage density capacitors of $Bi(Ni_{1/2}Ti_{1/2})O_3$-$PbTiO_3$ thin films with good temperature stability, J. Am. Ceram. Soc. 96 (7) (2013) 2061–2064.
[53] M.X. Zhou, R.H. Liang, Z.Y. Zhou, X.L. Dong, Superior energy storage properties and excellent stability of novel $NaNbO_3$-based lead-free ceramics with A-site vacancy obtained via a Bi_2O_3 substitution strategy, J. Mater. Chem. A Mater. Energy Sustain. 6 (37) (2018) 17896–17904.
[54] F. Li, K. Yang, X. Liu, J. Zou, J.W. Zhai, B. Shen, P. Li, J. Shen, B.H. Liu, P. Chen, K.Y. Zhao, H.R. Zeng, Temperature induced high charge-discharge performances in lead-free $Bi_{0.5}Na_{0.5}TiO_3$-based ergodic relaxor ferroelectric ceramics, Scr. Mater. 141 (2017) 15–19.
[55] J.M. Ye, G.S. Wang, M.X. Zhou, N.T. Liu, X.F. Chen, S. Li, F. Cao, X.L. Dong, Excellent comprehensive energy storage properties of novel lead-free $NaNbO_3$-based ceramics for dielectric capacitor applications, J. Mater. Chem. C Mater. Opt. Electron. Devices 7 (19) (2019) 5639–5645.